LANGMUIR

pubs.acs.org/Langmuir Article

Nickel Foam-Loaded $CoFe_2O_4$/CuS/RGO Electrode for a Bifunctional Device for Glucose Detection and Hydrogen Release

Bairui Tao,*[,‖] Chengyu Tao,[‖] Fengjuan Miao,* Peng Zhang,* and Paul K. Chu

Cite This: *Langmuir* 2025, 41, 30982−30993 Read Online

ACCESS | Metrics & More | Article Recommendations

ABSTRACT: Bad living habits, such as the lack of exercise, unhealthy food consumption, and insufficient sleep, cause health problems such as reduced blood glucose regulation ability and early onset of diabetes. At the same time, the pursuit of sustainable development requires renewable energy generation, and water splitting driven by solar, wind, hydro, and geothermal power is one of the viable techniques. Therefore, a bifunctional nanoelectrode with dual functions of sweat analysis and the hydrogen evolution reaction (HER) is of great significance in the prevention of diabetes and the development of green energy. Herein, a $CoFe_2O_4$/CuS/RGO composite electrode is fabricated on nickel foam (NF with a surface area of 1 cm^2) by simple digestion, chemical coprecipitation, and hydrothermal methods. The glucose redox and charge transfer processes have been systematically investigated. The results reveal that the composite not only has excellent glucose electrochemical activity but also can be used for hydrogen production. The detection boasts a glucose detection range of 1−5 mM, sensitivity of 1199 $\mu A\ mM^{-1}cm^{-2}$, signal-to-noise ratio of 3, and detection limit of 0.25 μM. As an electrode in a hydrogen evolution setup, it shows a current density of 10 mA cm^{-2} at an overpotential of 327 mV and a Tafel slope of 10.27 mV dec^{-1}.

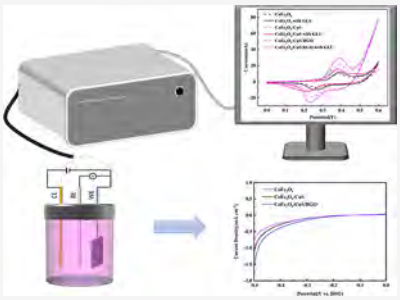

1. INTRODUCTION

The prevalence of diabetes has increased, and patients tend to be younger. The energy sector is also changing.[1] Hence, dual-function sensors for glucose detection and hydrogen evolution are of great significance in these two.[2,3] Common glucose sensors have some intrinsic drawbacks, such as interferences, low accuracy, and high cost,[4] and conventional enzymatic sensors tend to have poor stability and require complex preparation.[5] In this respect, electrochemical sensors have high sensitivity, fast response, low cost, good stability, and small volume requirement.[6] Traditional hydrogen production methods also have shortcomings, as they rely on fossil fuel, cause global environmental changes, and are expensive. Hydrogen production by water photoelectrolysis is expensive on the industrial scale due to the low photocatalytic efficiency and high energy consumption.[7] Hydrogen evolution using renewable biomolecules as raw materials can be carried out under mild conditions and has lower energy consumption and cost.[8]

In terms of glucose-sensitive materials, $CoFe_2O_4$ can be prepared by the coprecipitation method, which features simple operation and low equipment requirements, facilitating large-scale production. Its raw materials, iron and cobalt, are abundant in reserves and have stable prices. $CoFe_2O_4$ has a spinel structure, enabling electron energy transition, which contributes to electron transfer during glucose detection. Moreover, it exhibits electrocatalytic activity for glucose oxidation, catalyzing the oxidation of glucose to gluconic acid in an alkaline medium and generating current signals, with stable structure and long-lasting catalytic activity.[9,109] In the field of glucose detection and hydrogen evolution reaction (HER), existing materials have obvious limitations: the self-powered sensor reported by Zhu et al. is only limited to single-target analysis and relies on irreversible catalyst poisoning, which restricts its reusability;[11] the wearable sensor developed by Li et al. can detect uric acid and glucose in sweat, but the glucose detection depends on enzyme catalysis that is susceptible to environmental influences, and it requires precision-printed electrodes, increasing the complexity;[12] in addition, the single $CoFe_2O_4$ has limited catalytic activity in hydrogen evolution reaction.

The innovatively developed $CoFe_2O_4$/CuS/RGO composite material in this study realizes the integration of dual functions of nonenzymatic glucose detection and hydrogen evolution catalysis. It avoids irreversible loss through a nonenzymatic mechanism, overcomes the drawbacks of enzyme catalysis, and does not require precision-printed electrodes, making the preparation more convenient. The components of the composite material have significant synergistic effects: $CoFe_2O_4$ provides a catalytic basis with easily available raw

Received: June 11, 2025
Revised: October 29, 2025
Accepted: October 29, 2025
Published: November 12, 2025

https://doi.org/10.1021/acs.langmuir.5c02969
Langmuir 2025, 41, 30982−30993

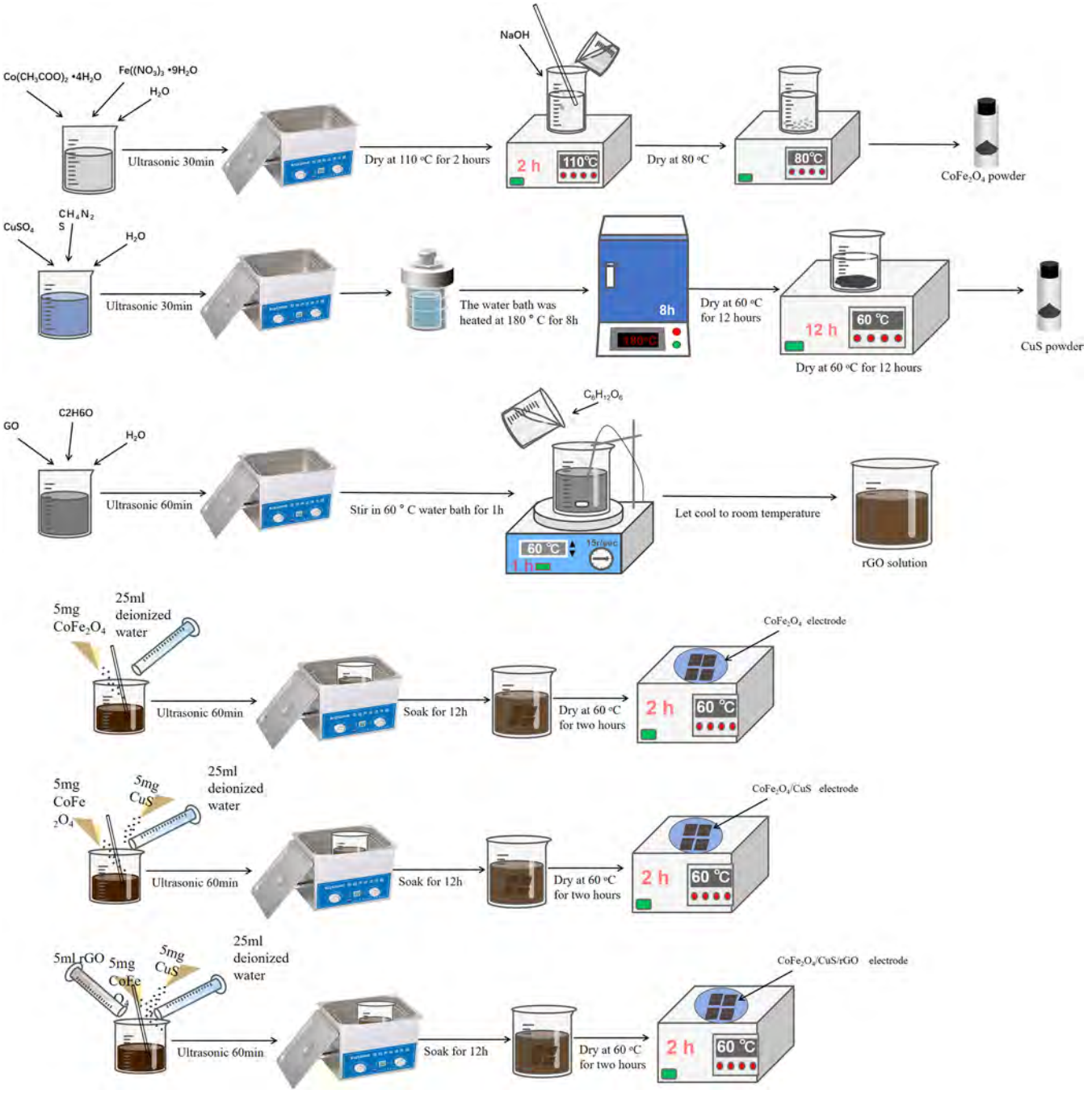

Figure 1. Preparation of $CoFe_2O_4$/CuS/RGO composites by digestive chemical coprecipitation, hydrothermal method, and annealing.

materials and simple preparation; CuS reduces the activation energy of hydrogen evolution and optimizes the electronic structure; and RGO provides electron transport channels, enhancing the performance and stability. This composite material provides new ideas for related fields.[13]

2. EXPERIMENTAL DETAILS

The synthesis of $CoFe_2O_4$/CuS/RGO is illustrated in Figure 1.[14] The $CoFe_2O_4$ nanoparticles were prepared by digestive chemical coprecipitation, while the CuS particles were prepared by a hydrothermal method and annealing. The reduced GO (RGO) solution was obtained by the glucose reduction of GO (GO). $CoFe_2O_4$, CuS, and RGO were combined to form $CoFe_2O_4$/CuS/RGO.

2.1. Materials and Reagents. The chemicals were used without purification, and deionized water (DI) was used to form the solutions. Cobalt acetate tetrahydrate $\{(CH_3COO)_2Co{\cdot}4H_2O\}$ was purchased from Aldrich (Shanghai, China). Ferric nitrate nonhydrate $\{Fe(NO_3)_3{\cdot}9H_2O\}$, NaOH, glucose, sucrose, lactose, fructose, and maltose were purchased from Kemer (Tianjin, China). Copper sulfate $CuSO_4$, thiocarrea (CH_4N_2S), and absolute ethanol (C_2H_6O) were provided by Aladdin (Shanghai, China); graphene oxide powder (GO) was purchased from XFNANO (Nanjing, China); ascorbic acid (AA), uric acid (UA), and dopamine (DA) were bought from Aladdin (Shanghai, China). Nickel foam (Ni) was obtained from Changsha Lipu New Material Co., Ltd. The foam thickness was 1.5 mm, the pore density was 100 holes per inch (PPI), and the surface density was 380 (gm^{-2}).

2.2. Preparation of $CoFe_2O_4$. First, according to the Co:Fe atomic ratio of 1:2, $Co(CH_3COO)_2{\cdot}4H_2O$ and $Fe(NO_3)_3{\cdot}9H_2O$ are

https://doi.org/10.1021/acs.langmuir.5c02969
Langmuir 2025, 41, 30982−30993

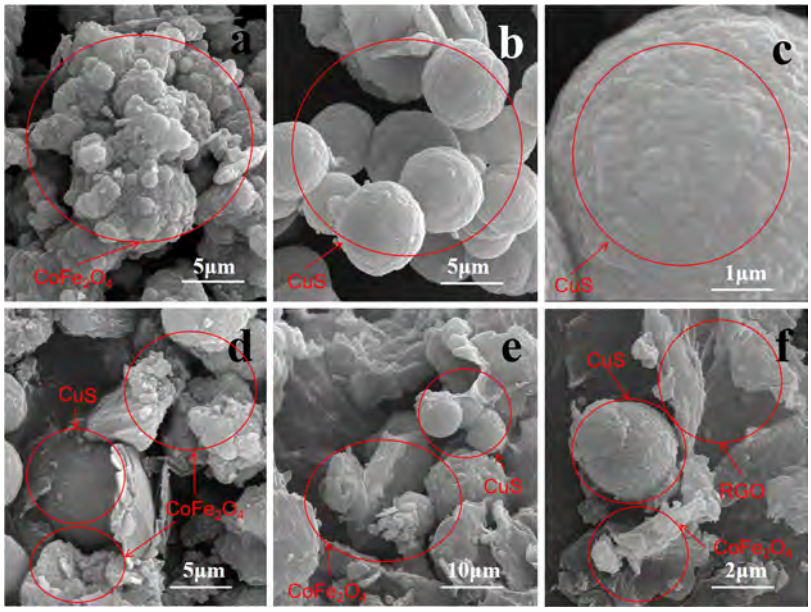

Figure 2. SEM images: (a) $CoFe_2O_4$, (b, c) CuS, (d) $CoFe_2O_4$/CuS/RGO, and (e, f) $CoFe_2O_4$/CuS/RGO after CV testing.

weighed and dissolved in deionized water to form a mixed solution. Then, slowly pour it into a well-stirred NaOH solution until no more precipitate is formed. Continue stirring for a few more minutes to ensure the reaction is fully carried out. Next, transfer the reaction mixture to a high-pressure reactor with a poly(tetrafluoroethylene) inner lining, and perform digestion treatment at 110 °C for 120 min (with a stirring speed of 300 r/min) to allow the particles to grow and transform into spherical structures. After digestion, filter to obtain gel-like precipitates, and repeatedly wash with deionized water until the pH value of the filtrate becomes neutral. Dry in air at 80 °C to form powder samples. Disperse the powder in ethanol by ultrasonication (with an ultrasonic power of 300 W and an ultrasonic time of 30 min), centrifuge, rewash with ethanol, and then dry to finally obtain monodisperse $CoFe_2O_4$ nanoparticles. Weigh 5 mg of $CoFe_2O_4$ nanoparticles and dissolve them in 25 mL of deionized water, ultrasonic to achieve uniformity (with an ultrasonic power of 200 W and an ultrasonic time of 20 min), to obtain a uniformly distributed $CoFe_2O_4$ suspension solution. Immerse the prewashed foam nickel (NF) with deionized water, hydrochloric acid, and ethanol in the suspension solution, place it in a dark environment and let it stand for 24 h, then remove the foam nickel, air-dry at 60 °C for 30 min, and obtain the $CoFe_2O_4$ nanoparticle electrode.

2.3. Preparation of $CoFe_2O_4$/CuS. $CuSO_4$ (18 mg) and thiourea (18 mg) were dissolved in 70 mL of deionized water, sonicated for 15 min until full dissolution, stirred for 30 min at room temperature, and transferred to a Teflon-lined autoclave. After sealing the autoclave, the reaction proceeded for 8 h at 180 °C. After the autoclave was cooled to room temperature, the solution was removed and dried in air at 80 °C to obtain the monodispersed CuS nanoparticles. Five mg of $CoFe_2O_4$ nanoparticles and 5 mg of CuS nanoparticles were dissolved in 25 mL of deionized water and sonicated to form a homogeneous suspension. The precleaned nickel foam (NF) was immersed in the suspension in the dark for 24 h. Afterward, the nickel foam was removed and air-dried at 60 °C for 30 min to obtain the $CoFe_2O_4$/CuS nanocomposite.

2.4. Preparation of $CoFe_2O_4$/CuS/RGO. GO (50 mg) was dispersed in 10 mL of deionized water and sonicated for 60 min, after which absolute ethanol (40 mL) was added to obtain a GO solution with a concentration of 1 mg/mL (total volume 50 mL). The glucose powder (0.3 g) was placed in 5 mL of deionized water, and the solution was sonicated for 5 min to prepare the glucose solution. The GO dispersion was heated in a 60 °C water bath for 60 min under magnetic stirring, and the glucose solution was dropped slowly during the heating process. After completion of the reaction, the mixture was cooled to room temperature to obtain the reduced graphene oxide (RGO) solution. The $CoFe_2O_4$ nanoparticles (5 mg) and CuS nanoparticles (5 mg) were dissolved in 25 mL of deionized water, and the GO solution (5 mL) was added and sonicated to form a uniform suspension. The precleaned nickel foam (NF) was immersed in the suspension in the dark for 24 h. Subsequently, the nickel foam was removed and air-dried at 60 °C for 30 min to obtain the $CoFe_2O_4$/CuS/RGO nanocomposite.

2.5. Characterization. The morphology and microstructure of $CoFe_2O_4$/CuS/RGO were examined by scanning electron microscopy (Tescan MIRA 3XMU) and transmission electron microscopy (JEM 2100F). X-ray diffraction (Bruker Miniflex 600, Al K_α source) and energy-dispersion X-ray spectroscopy (EDS) were used to determine the structure. X-ray photoelectron spectroscopy (XPS) was performed on a VG Scientific ESCALAB250 (1 keV argon sputtering, 30° incidence Angle). A CHI760E electrochemical workstation was used to perform cyclic voltammetry (CV) and amperometry in 1 M KOH at room temperature. The three-electrode configuration consists of the $CoFe_2O_4$/CuS/RGO electrode, Pt electrode, and Ag/AgCl electrode as the working electrode, counter electrode, and reference electrode, respectively.

3. RESULTS AND DISCUSSION

3.1. Materials Characterization. The microstructure and morphology of $CoFe_2O_4$/CuS/RGO were analyzed by SEM (Figure 2). Figure 2(a) showcases the scanning electron microscopy (SEM) image of $CoFe_2O_4$, where the particles take on an aggregated morphology, with relatively irregular shapes and a certain extent of agglomeration.[15] Figure 2(b,c) exhibits the SEM images of CuS: in Figure 2(b), CuS displays a uniform spherical structure with a relatively consistent size distribution; while Figure 2(c), at a higher magnification, reveals that the surface of CuS spheres is constituted by smaller nanoparticles, forming a hierarchical structure.[16] Figure 2(d) is the SEM image of the $CoFe_2O_4$/CuS/RGO composite, from which it can be observed that $CoFe_2O_4$ and CuS particles are integrated with reduced graphene oxide (RGO), and CuS spheres as well as $CoFe_2O_4$ particles are distributed on or around the RGO sheets, indicating the successful combination of the three components.[17] Figure 2(e,f) depicts the SEM images of the composite after cyclic voltammetry (CV) testing,

https://doi.org/10.1021/acs.langmuir.5c02969
Langmuir 2025, 41, 30982−30993

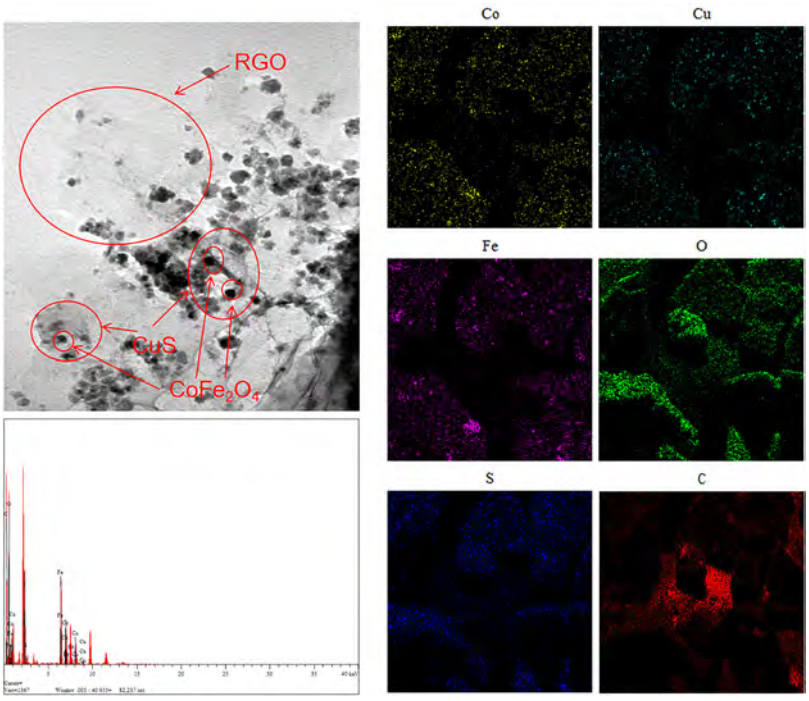

Figure 3. TEM image of $CoFe_2O_4$/CuS/RGO and (b−h) EDS elemental maps.

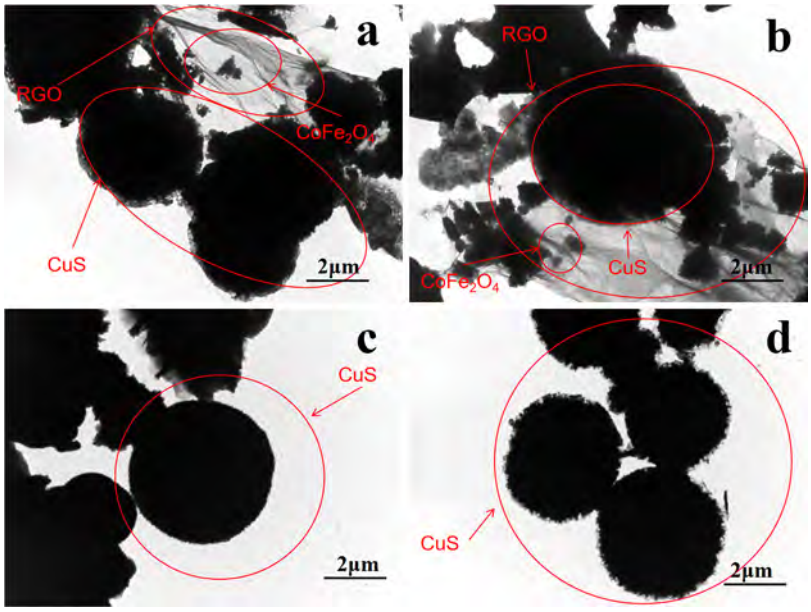

Figure 4. TEM image of $CoFe_2O_4$/CuS/RGO composite after CV testing.

and its morphology has undergone some changes compared with the original composite. Owing to the electrochemical processes during the CV testing, the distribution and interaction among CuS, $CoFe_2O_4$, and RGO have been altered.

The morphology of $CoFe_2O_4$/CuS/RGO was observed by transmission electron microscopy (TEM). The spherical structures of granular $CoFe_2O_4$crystals, RGO lamellae, and CuS can be clearly observed in Figure 3a. Figure 4 shows the TEM characterization of the composite after CV testing. $CoFe_2O_4$ and CuS attached to the RGO lamellae can be clearly seen in Figure 4a,b, while Figure 4b is the magnified image. The high conductivity and large specific surface area of RGO provide good support and dispersion for $CoFe_2O_4$/CuS.[18] Figure 4c,d shows a magnified image of the local Cus spherical structure. CuS, with its specific crystal surface and atomic arrangement, can expose more active sites. These active sites play an important role in catalytic reactions, which can adsorb reactant molecules and promote chemical reactions, thereby improving the efficiency and selectivity of the catalytic reactions.[19] Figure 3c−h shows the presence of Co, Fe, S, Cu, O, and C, confirming the uniform distribution of Co, Fe, and Cu in the composite nanomaterials $CoFe_2O_4$/CuS/RGO.

Figure 5a shows the XPS survey spectrum, revealing the Cu 2p, Ni 3p, Co $2p_{3/2}$, Co $2p_{1/2}$, and the O 1_s, C 1s, and S 2p peaks. In the C 1s spectrum in Figure 5b, the peak at 284.8 eV is attributed to the C−C bond, the peak at 286.1 eV

https://doi.org/10.1021/acs.langmuir.5c02969
Langmuir 2025, 41, 30982−30993

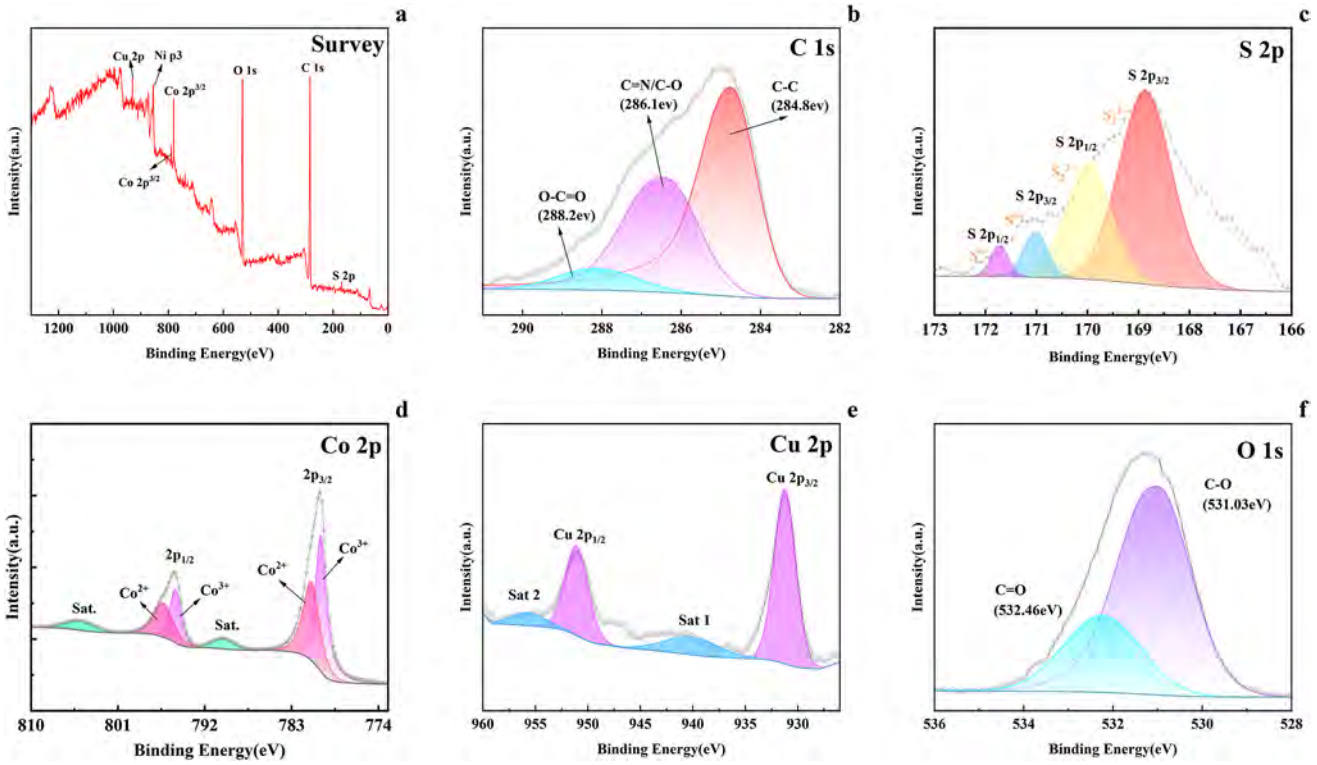

Figure 5. XPS patterns of $CoFe_2O_4$/CuS/RGO composites.

corresponds to C═N/C−O, and that at 288.2 eV is O−C═O.[20] As shown in the S 2p spectrum in Figure 5c, multiple peaks such as S $2p_{3/2}$, S $2p_{1/2}$, etc. are observed.[21] Figure 5d shows the Co 2p spectrum, revealing Co $2p_{3/2}$ and Co $2p_{1/2}$ peaks at 781.51 and 797.36 eV, peaks of Co^{2+} and Co^{3+}, and some satellite peaks (Sat). Co^{2+} and Co^{3+} are observed, indicating Co oxidation states of +2 and +3. The satellite peak arises from multiple scattering during the electronic transition.[22] Figure 5e shows the Cu 2p spectrum, revealing Cu $2p_{3/2}$ and Cu $2p_{1/2}$ peaks at 932.64 and 951.87 eV, as well as satellite peaks Sat 1 and Sat 2.[23] As shown in Figure 5f, the peak at 531.03 eV corresponds to C−O, and that at 532.46 eV corresponds to C═O.[24]

Figure 6a,b shows the diffraction (XRD) patterns of the crystals against X-rays before and after CV testing, respectively. In Figure 6a, diffraction peaks marked with red dots (such as crystal planes (002), (102), (105), (108), (202), (218)) belong to CuS. The internal copper atoms and sulfur atoms are arranged regularly and periodically, and the diffraction peak position and intensity of these crystal planes are highly matched with the CuS standard crystal data, confirming the existence of the CuS phase in the sample. From the structural point of view, the appearance of peaks indicates that the CuS crystal lattice is well periodic, the atoms are ordered, and the crystal structure integrity is high. The diffraction peaks marked by green diamonds (such as crystal planes (120) and (121)) correspond to $CoFe_2O_4$. "A ferrite of spinel structure arranged in a specific lattice by Co^{2+}, Fe^{3+}, and $O2^{-}$." The formation of this crystal phase is verified by the presence of characteristic diffraction peaks, and the peak positions are consistent with the standard database, indicating that the crystal structure of the synthesized $CoFe_2O_4$conforms to the theoretical expectation without obvious distortion of the lattice parameters. Some of the main peaks have a higher intensity, which corresponds to

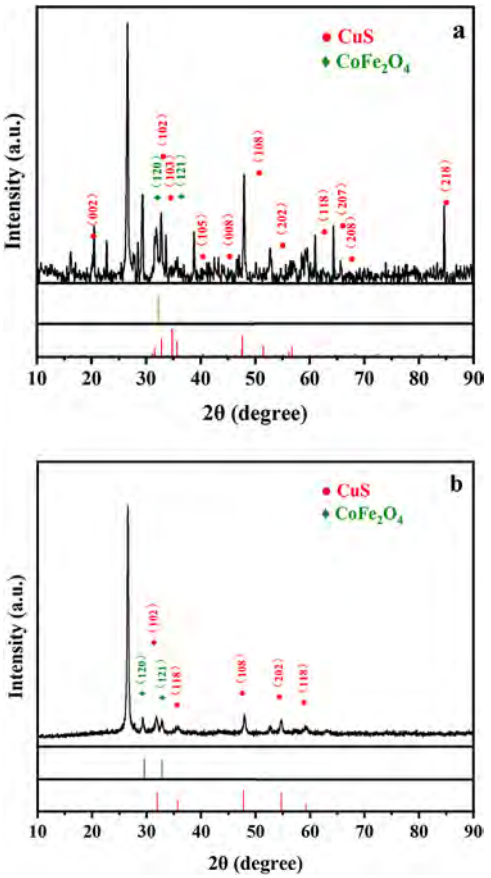

Figure 6. XRD patterns of $CoFe_2O_4$/CuS/RGO composites.

the strong scattering ability of atoms in the crystal plane, or the crystal orientation is more concentrated in this direction. At

https://doi.org/10.1021/acs.langmuir.5c02969
Langmuir 2025, 41, 30982−30993

the same time, the width and intensity of the peak indicate high crystallinity, indicating that the crystal structure is intact and there are few defects.[24] This XRD image makes the coexistence of CuS and $CoFe_2O_4$ in the sample.

3.2. Electrochemical Glucose Sensing. Figure 7 presents CV curves of $CoFe_2O_4$-based composites with 0.2 mM glucose

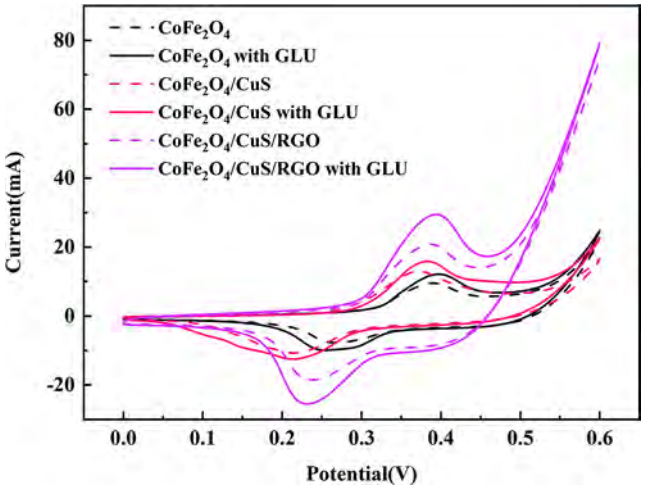

Figure 7. CV curves of $CoFe_2O_4$, $CoFe_2O_4$/CuS, and $CoFe_2O_4$/CuS/RGO with and without 1 mM glucose.

(GLU) in 1 M KOH, showing kinetic differences. A saturated Ag/AgCl reference electrode and a Pt counter electrode were used. The unmodified $CoFe_2O_4$ (first curve) exhibits low peak current due to limited electron conduction and insufficient active sites (Co^{2+}/Co^{3+}, Fe^{2+}/Fe^{3+}), weakening glucose catalytic oxidation. After adding CuS and RGO (second/third curves), oxidation current peaks rise significantly, consistent with the composite's glucose detection mechanism: CuS provides Cu^{+}/Cu^{2+} redox couples as auxiliary catalytic sites to enhance adsorption/oxidation activity, while RGO's high conductivity and large surface area improve electron transfer (reducing charge resistance) and disperse active components. Their synergy boosts electron transfer efficiency and active site exposure.[25] GLU introduction further alters the current response in $CoFe_2O_4$ /CuS/RGO: GLU optimizes intermediate adsorption via surface −OH/−COOH, balancing interaction strength (avoiding overly strong/weak adsorption) to refine oxidation pathways. Mechanistically, this promotes glucose dehydrogenation at Co^{2+}/Co^{3+}, Fe^{2+}/Fe^{3+}, and Cu^{+}/Cu^{2+} sites (producing gluconic acid and electrons), with electrons rapidly transferred via RGO.[26] This causes peak potential negative shift (reduced overpotential), confirming excellent glucose activity—matching its performance: 1 μM−5 mM detection range, 1199 μA $mM^{-1}cm^{-2}$ sensitivity, 0.25 μM detection limit (S/N = 3).

Figure 8a shows the CV curves at scanning rates of 10, 30, 50, 80, and 100 mV/s. As the scanning rates increase, the response is enhanced, and the peak current increases due to the larger charge transfer rates. However, a large scanning rate aggravates the polarization effect, which is manifested as an increase in the potential difference between the redox peaks (ΔE_p). It is because the diffusion process cannot keep up fully with the electron transfer rate at a high scanning rate, leading to a higher concentration and electrochemical polarization.[25] According to curve fitting, there is a good relationship between the peak current (Ip) and the square root of the scanning rate (v). The linear regression equations in Figure 8b are $y = 1.901x + 0.00327$ and $y = 1.64381x - 0.00247$ with high R^2 values of 0.99741 and 0.99667. The good linear relationships suggest that the electrochemical reaction is controlled by diffusion and the Randles−Sevcik relationship. The slope of the fitted curve reflects the reaction kinetics with a larger slope translating into a faster reaction. In addition, the separation of the redox peaks increases with scanning rates, indicating a decreased reversibility. At smaller scanning rates, ΔE_p is small, and the system is close to the reversible or quasi-reversible state. However, at high scanning rates, the ΔE_p increases, and the reaction is gradually controlled by kinetics. This conclusion is supported by the fitted curves, which show that the polarization effects and kinetic control influence the response more significantly at high scanning rates. At small scanning rates, the system shows good reversibility and small polarization, whereas at high scanning rates, polarization increases and reversibility decreases.[27] Figure 8c shows the response in the presence of different glucose concentrations (0 to 0.08 mM). The fitted equation is $y = 1.25x + 12.99$ with $R^2 = 0.99039$. Figure 8d shows that with increasing glucose concentrations, the currents increase linearly as better electron transfer increases the current.[28] The excellent R^2 values confirm the reliability and consistency of the detection of glucose.

As shown in Figure 9, $CoFe_2O_4$/CuS/RGO shows the smallest radius of the impedance arc, implying the lowest charge transfer resistance (R_{ct}).[29] A smaller R_{ct} translates to more efficient charge transfer between the electrode and the electrolyte. The R_{ct} value of $CoFe_2O_4$/CuS is less than that of $CoFe_2O_4$, indicating that CuS improves the charge transfer ability. However, the addition of RGO reduces R_{ct} because the high conductivity and large specific surface area of RGO facilitate electron transport and ion diffusion. All of the all, the results indicate that $CoFe_2O_4$/CuS/RGO has the optimal electrochemical properties.

Figure 10a shows the current versus time curves for different glucose concentrations (1 μM to 10 mM). The currents rise with concentrations, and Figure 10b shows the linear fitted curve of the current versus concentration. In the concentration range of 10−200 μM, which is the normal range for a healthy person,[30] the fitted equation is I (mA) = 0.01199C(μM) − 0.51298 with an excellent R^2 of 0.99545. Hence, the electrochemical sensor responds linearly in this concentration range. The current−time curve in Figure 10a shows the electrochemical response at different concentrations, and the current increases with concentration, as shown in Figure 10b. The $CoFe_2O_4$/CuS/RGO composite shows a glucose detection range of 1 μM−5 mM, a sensitivity of 1199 μamM^{-1} cm^{-2}, a signal-to-noise ratio of 3, and a detection limit of 0.25 μM. Table 1 compares the electrochemical data of the $CoFe_2O_4$/CuS/RGO composite electrode with other sensors and validates that $CoFe_2O_4$/CuS/RGO delivers excellent performance.Table 1 compares the electrochemical analysis data of the $CoFe_2O_4$/CuS/RGO composite electrode with different sensors, and the $CoFe_2O_4$/CuS/RGO composite electrode has excellent performance.

Figure 11 shows the response in the presence of various electroactive biomolecules, such as glucose, lactose, fructose, dopamine (DA), and uric acid (UA). The left curve in Figure 11a shows the results in the presence of 10 μM glucose, 1 mM lactose, 1 mM fructose, 1 mM DA, and 1 mM UA, revealing that the response to 10 μM glucose is dominant compared to

https://doi.org/10.1021/acs.langmuir.5c02969
Langmuir 2025, 41, 30982−30993

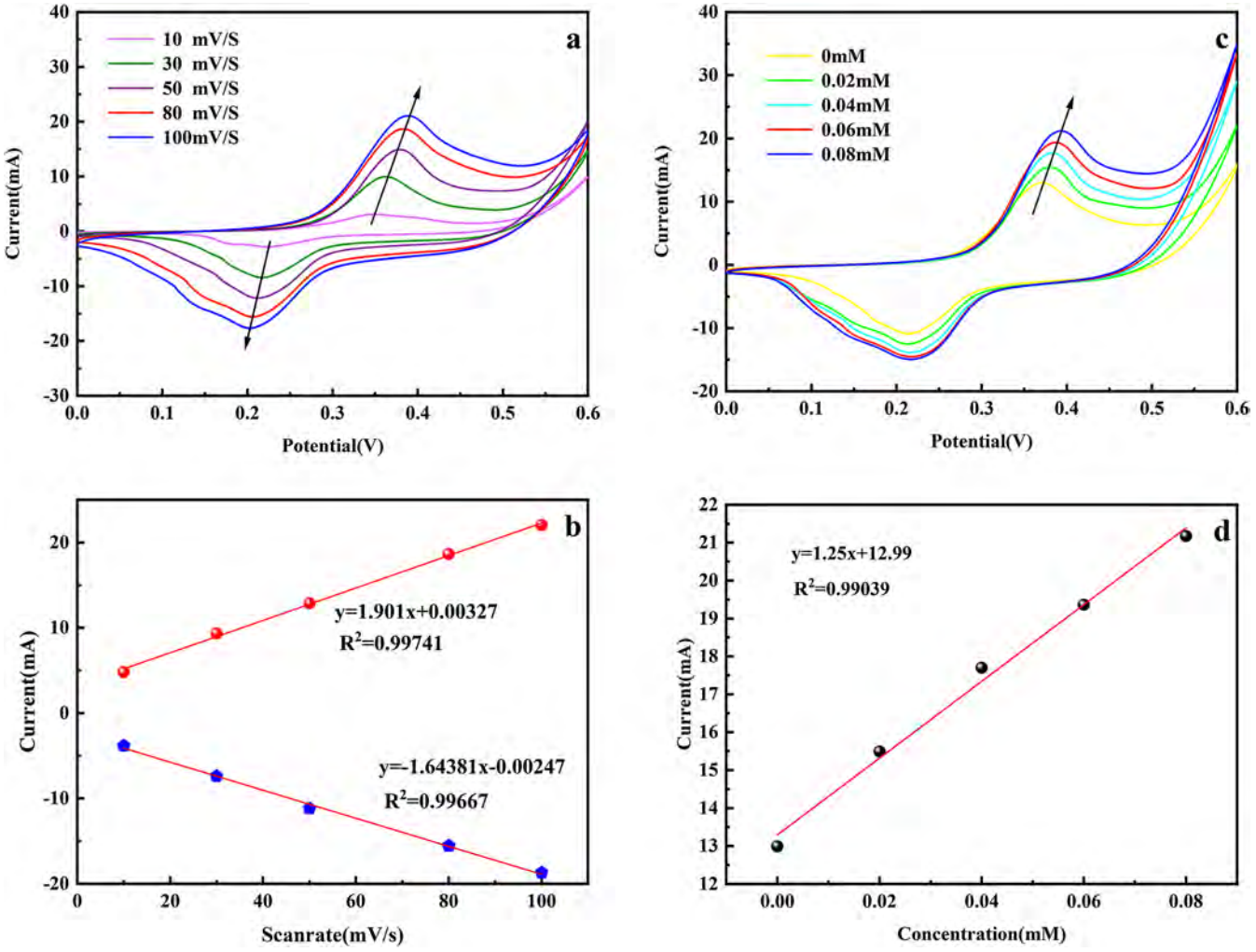

Figure 8. (a) CV curves of $CoFe_2O_4$/CuS/RGO composites at scanning rates between 10 and 100 mV (increments of 20 mV, 1 mM glucose); (b) CV curves of $CoFe_2O_4$/CuS/RGO composites at 0 to 0.08 mM glucose concentrations (increment of 0.02 mM glucose, 30 mV sweeping rate); (c) fitted peak currents for different scanning rates; (d) fitted peak currents for different concentrations.

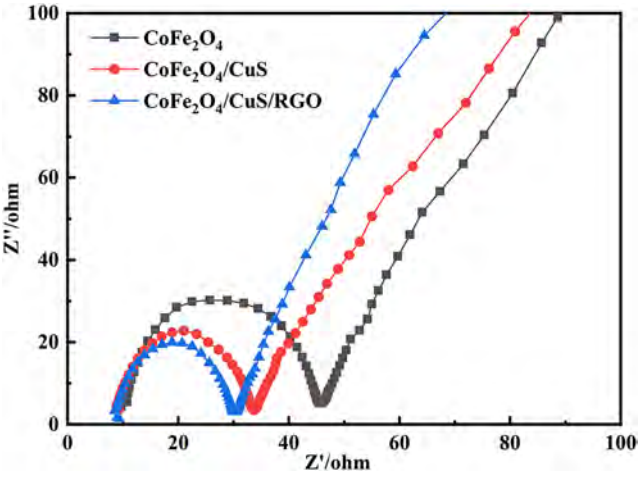

Figure 9. EIS Nyquist plots of $CoFe_2O_4$, $CoFe_2O_4$/CuS, and $CoFe_2O_4$/CuS/RGO.

other molecules, such as lactose, fructose, DA, and UA. The normalized response percentages in Figure 11b are 15.3, 13.1, 11.1, 7.8, and 5.4%, respectively, indicating high glucose selectivity arising from the specific recognition and efficient catalytic oxidation of glucose. The lower response to the other molecules indicates insignificant cross-reactivity from interfering substances, and it is emphasized that high selectivity is crucial to glucose measurement in complex biological samples.

3.3. Hydrogen Evolution Reaction. Figure 12a shows the CV curve of $CoFe_2O_4$, revealing a low current response and a small electrochemically active surface area, resulting in relatively poor electrochemical properties. The curve of the $CoFe_2O_4$/CuS composite in Figure 12b shows a higher response, indicating that CuS improves the electrochemical activity. The addition of CuS reduces the charge transfer resistance and improves the charge transport efficiency. The curve of the $CoFe_2O_4$/CuS/RGO composite in Figure 12c shows the highest current and widest electrochemical window because reduced graphene oxide (RGO) enhances the conductivity and electrochemical properties.[36] From the perspective of CDL, the high conductivity and large surface area of RGO help to reduce the charge transfer resistance and promote more efficient charge transport.[37] The specific capacitance values of the three materials are also provided in Figure 12d, and the highest specific capacitance of $CoFe_2O_4$/CuS/RGO is 65.4 mF/cm^2, which further confirms its excellent electrochemical performance As an important parameter for measuring the surface active area of materials,

https://doi.org/10.1021/acs.langmuir.5c02969
Langmuir 2025, 41, 30982−30993

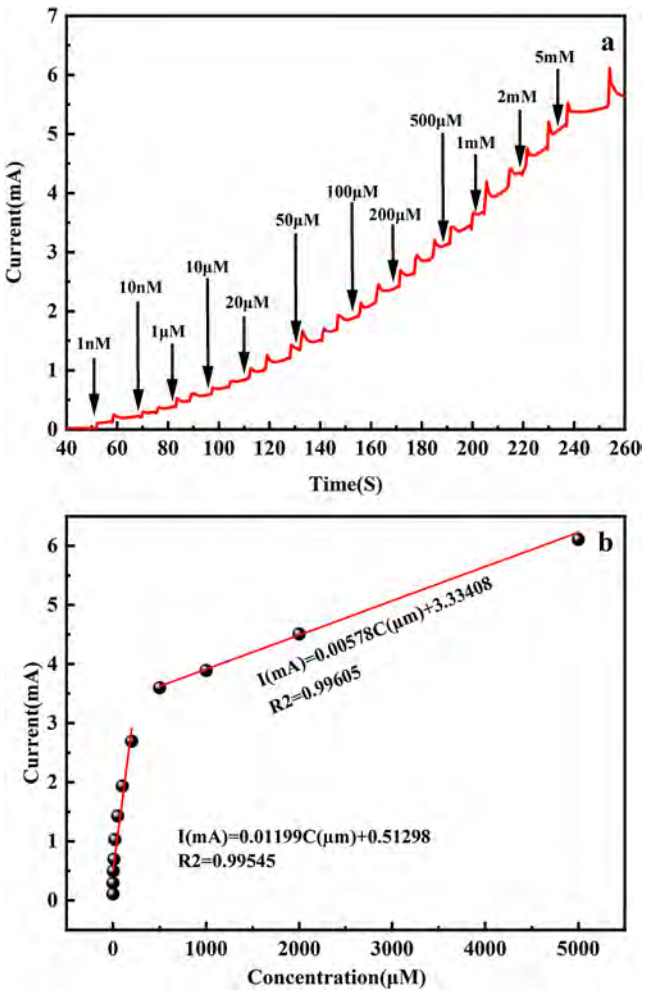

Figure 10. (a) Current−time relationship of the $CoFe_2O_4$/CuS/RGO electrode in the presence of glucose; (b) fitted linear relationship of current versus glucose concentration.

the electrochemical active surface area (ECSA) is usually calculated using the C_{dl} of the electrode and the specific capacitance (C_s) per unit area. The calculation formula is eq 1.

$$\mathrm{ECSA} = \frac{C_{dl}}{C_s} \tag{1}$$

Where C_s is typically calculated by eq 2.

$$C_S = \frac{It}{SV} \tag{2}$$

Here, I is the charge−discharge current, t is the discharge time, S is the geometric area of the electrode, and ΔV is the potential window. According to eq 3 derived from cyclic voltammetry (CV) curves.

$$\int_{V_1}^{V_2} I(v)\mathrm{d}v = \int_{V_1}^{V_2} C_S k S \mathrm{d}v \tag{3}$$

where V_2 is the highest scanning voltage, V_1 is the initial scanning voltage, and K is the scanning rate. It can be concluded as eq 4.

$$C_S = \frac{A}{2(V_2 - V_1)Sk} \tag{4}$$

where A is the absolute area of the CV curve, and V_2-V_1 is the potential window.

For the $CoFe_2O_4$/CuS/RGO composite electrode, the glucose detection sensitivity is 1199 μA mM^{-1} cm^{-2}, and the electrochemically active surface area (ECSA) is calculated as 7.91. The difference between sensitivity and ECSA not only reflects the structural supporting role of the RGO carrier in improving the dispersibility of $CoFe_2O_4$ and CuS, but also reveals how the component ratio of $CoFe_2O_4$, CuS, and RGO regulates the electronic structure through chemical mechanisms and affects the number of electrocatalytic active sites for glucose. The optimized component ratio in this experiment achieves an optimal balance between structural uniformity and the electronic synergistic effect, providing an ideal interface environment and charge transfer conditions for efficient electrochemical oxidation of glucose. This is also the key reason why the electrode can achieve a wide detection range of 1 μM to 5 mM and a low detection limit of 0.25 μM.

Figure 13 shows the differences in electrochemical performance among $CoFe_2O_4$, $CoFe_2O_4$/CuS, and $CoFe_2O_4$/CuS/RGO in the hydrogen evolution reaction (HER). The LSV polarization curves in Figure 13a reveal that $CoFe_2O_4$ exhibits a relatively high overpotential and low current density, resulting in poor HER activity. This is attributed to the limited number of active sites and low electron transfer efficiency, which hinder the Volmer step ($H^+ + e^- \rightarrow H^*$) and subsequent hydrogen desorption process. The polarization curve of $CoFe_2O_4$/CuS presents a lower overpotential and higher current density, indicating that the introduction of CuS effectively enhances the HER activity. Mechanistically, the additional active sites (Cu^+/Cu^{2+} redox couples) provided by CuS can promote the adsorption of H^+ in the Volmer step, and regulate the charge transfer efficiency to accelerate the electron transfer to the adsorbed H^+, thereby efficiently facilitating the Heyrovsky step. The polarization curve of $CoFe_2O_4$ /CuS/RGO demonstrates the optimal performance, with the lowest overpotential and highest current density. RGO, relying on its high conductivity and large specific surface area, can efficiently transfer electrons to the active sites of $CoFe_2O_4$ and CuS, reduce the charge transfer resistance, and increase the exposure of active sites, synergistically accelerating the rates of proton adsorption and H_2 generation. The Tafel slope analysis in Figure 13b further verifies the above results: the Tafel slopes of

Table 1. Comparison of the Properties of CoFe2O4/CuS/RGO with Those of Previously Reported Glucose Sensors

electrodes	range (mM)	sensitivity (μA$mM^{-1}cm^{-2}$)	detection limit (μM)	Refs
NiCu	0.01−12	42.3	0.5	31
CuS-rGO/g-C_3N_4	0.001−10	50.6	0.1	32
Ni_3C/Ni	0.001−0.065	299.4	0.28	33
AuNPs/$Ni(OH)_2$NS	0.002−6		0.66	34
Co_3O_4/NiO	0.01−9.055	2477	0.17	35
$CoFe_2O_4$/CuS/RGO	0.00001−5	1199	0.25	our work

https://doi.org/10.1021/acs.langmuir.5c02969
Langmuir 2025, 41, 30982−30993

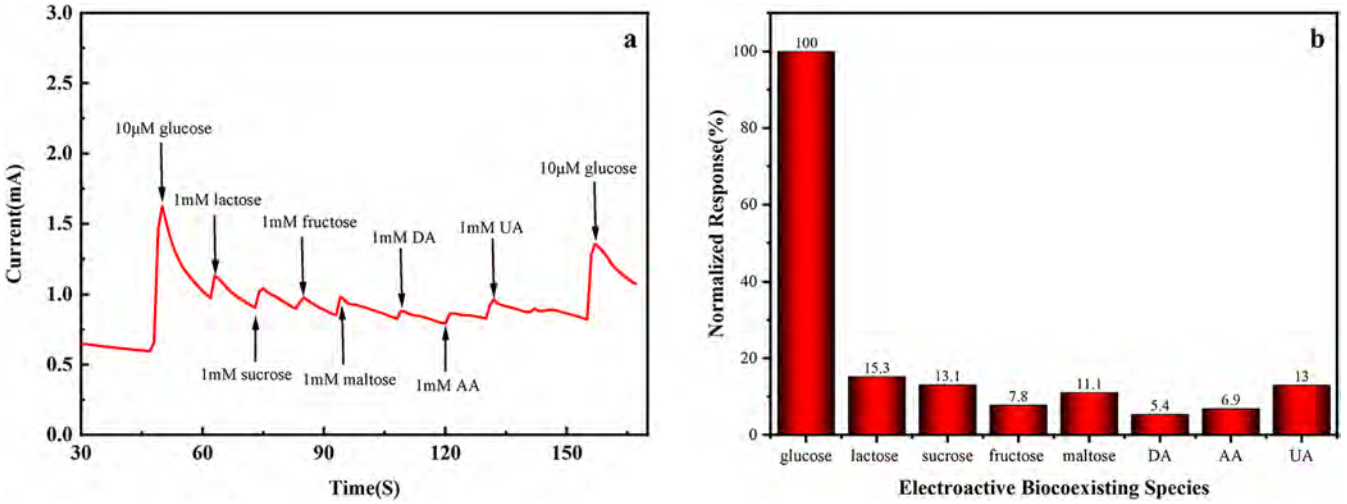

Figure 11. (a) $i-t$ curves of $CoFe_2O_4$/CuS/RGO in the presence of 10 μM glucose and interferences added to 1 M KOH; (b) comparison of the current increments between glucose and interferences.

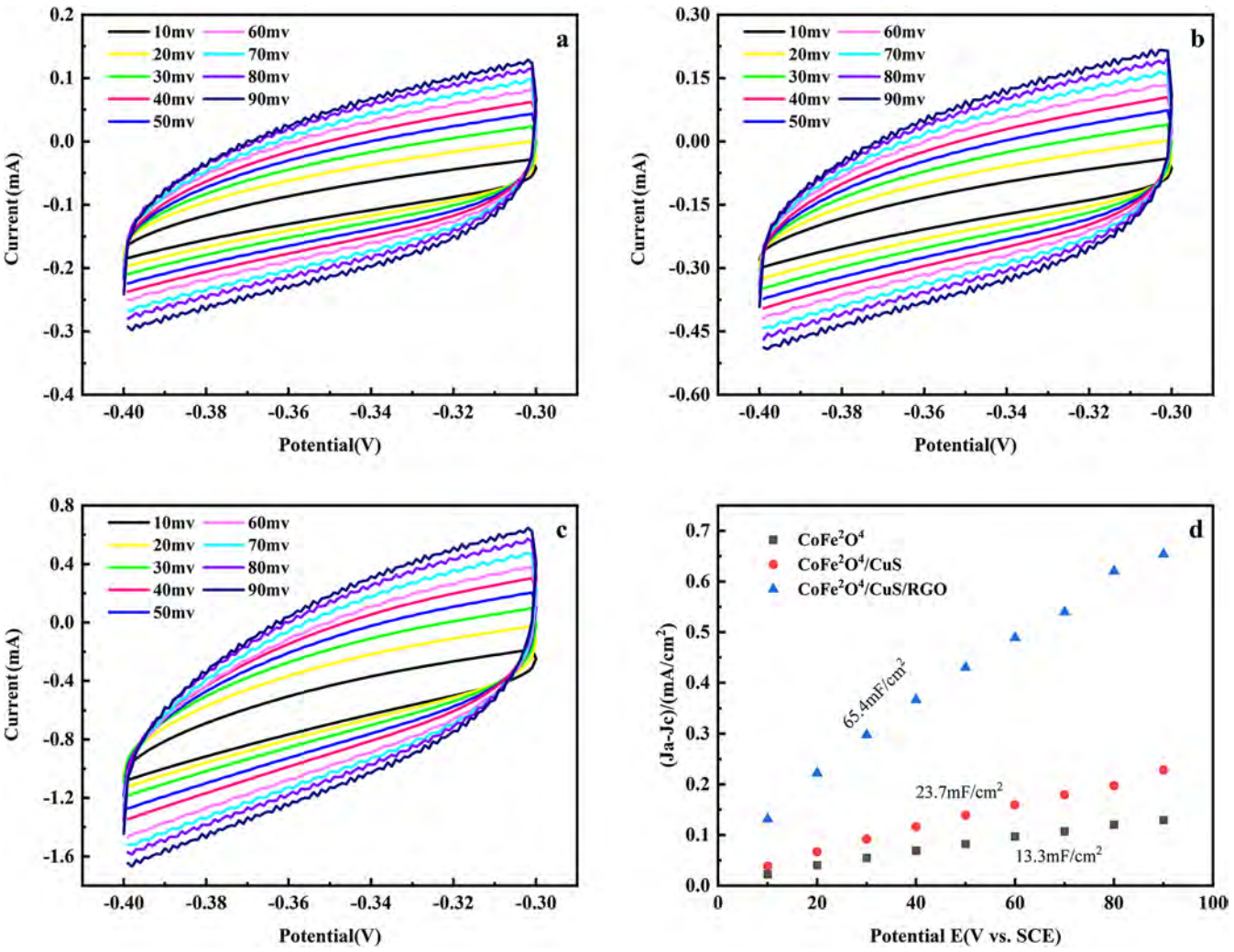

Figure 12. (a) Cyclic voltammograms of (a) $CoFe_2O_4$, (b) $CoFe_2O_4$/CuS, and (c) $CoFe_2O_4$/CuS/RGO; (d) linear fits of capacitive current versus scanning rates (10−90 mV/s).

$CoFe_2O_4$, $CoFe_2O_4$/CuS, and $CoFe_2O_4$/CuS/RGO are 18.08, 17.22, and 10.27 mV dec^{-1}, respectively. Among them, $CoFe_2O_4$/CuS/RGO has the smallest Tafel slope, indicating that it has the fastest HER kinetics and is dominated by the Heyrovsky step, which fully confirms the key optimization

https://doi.org/10.1021/acs.langmuir.5c02969
Langmuir 2025, 41, 30982−30993

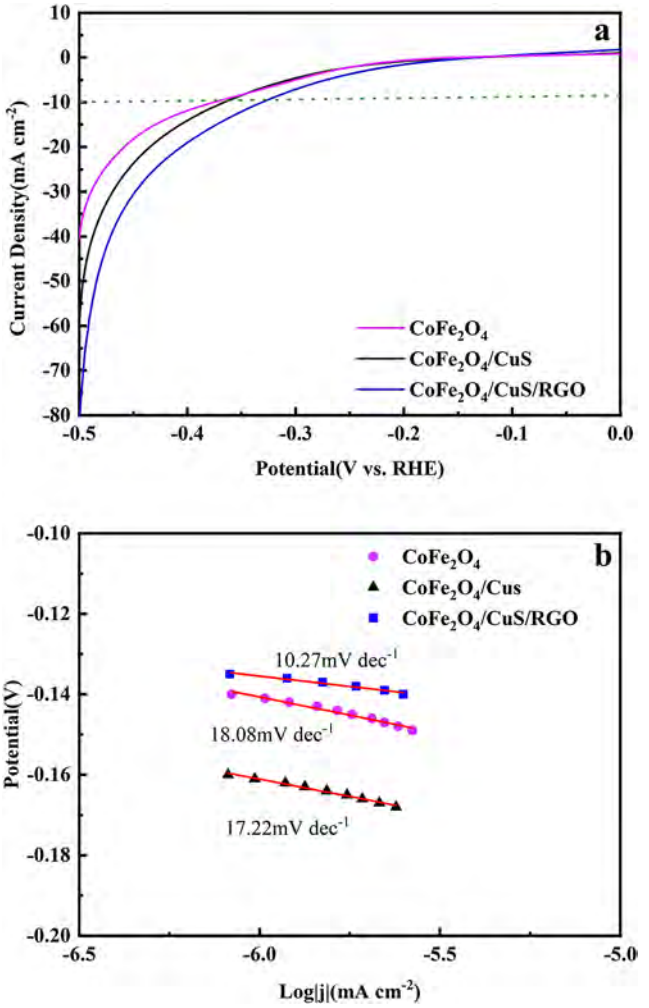

Figure 13. (a) Polarization curves of $CoFe_2O_4$, $CoFe_2O_4$/CuS, and $CoFe_2O_4$/CuS/RGO and (b) Tafel slope.

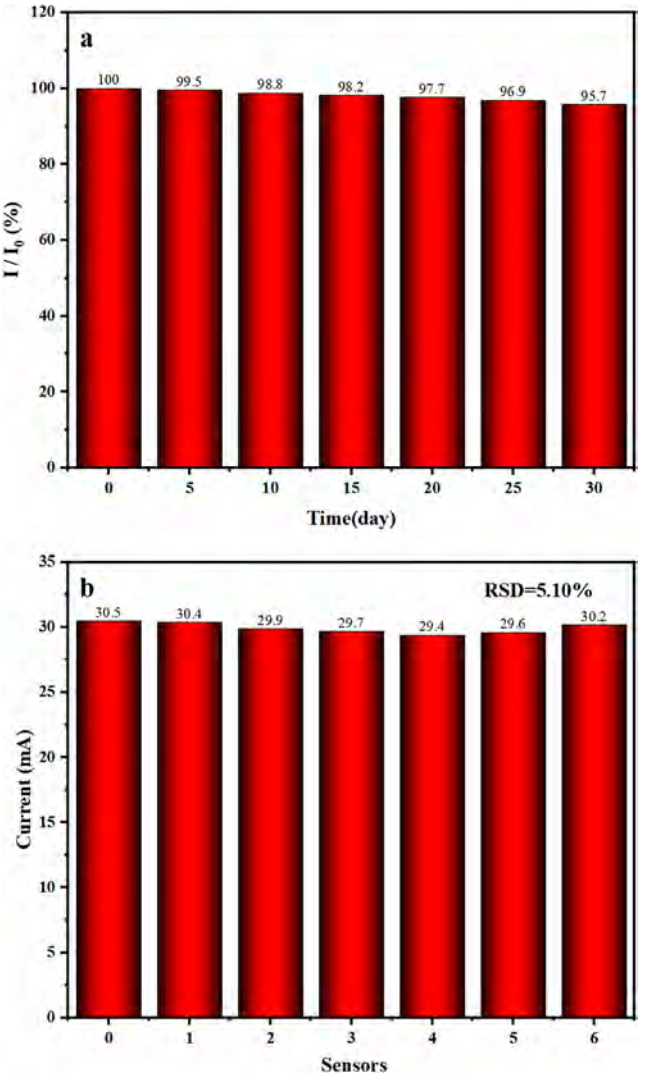

Figure 14. (a) CV peak current was measured in six sensors prepared using the same method with the addition of 2 mM glucose; (b) current density response to glucose was measured every 5 days for 30 days.

effect of component synergy on the hydrogen evolution pathway.[32]

For the practical evaluation of the $CoFe_2O_4$/CuS/RGO sensor's reproducibility and long-term stability: Figure 14a depicts long-term stability, with the current density relative to the initial value (I/I_0) decreasing gradually over 30 days but remaining at ~95.7%, showing slow performance attenuation and good long-term stability. Figure 14b shows current responses (in mA) of 6 sensors (numbered 0−6) and an RSD of 5.10%, reflecting good batch-to-batch consistency and reproducibility, ensuring stable performance in sensing applications.

4. CONCLUSIONS

The $CoFe_2O_4$/CuS/RGO composite electrode delivers excellent performance in glucose sensing and the hydrogen evolution reaction (HER). In glucose sensing, it shows a detection range of 1 μM−5 mM, a sensitivity of 1199 μA mM^{-1} cm^{-2}, and a detection limit of 0.25 μM. CuS improves the conductivity and catalytic activity, while RGO enhances electron transport and selectivity, thus rendering the electrode resistant to interferences in complex biological samples. The coordination of Fe^{3+} and Co^{2+} with glucose hydroxyl groups decreases the oxidation activation energy. Furthermore, the large specific surface area and good electron transport of RGO enhance the electrochemical properties, resulting in a linear response and stability in spite of low glucose concentrations. In the hydrogen evolution reaction, the composite achieves a current density of 10 mA cm^{-2} at an overpotential of 327 mV and a Tafel slope of 10.27 mV dec^{-1}. The high conductivity of RGO and semiconducting characteristics of CuS improve the HER kinetics, enabling the production of hydrogen at low overpotentials. Moreover, the RGO enhances the stability of the composite and ensures long-term catalytic activity. This dual-functional electrode has a large potential in diabetes monitoring and clean energy development.

AUTHOR INFORMATION

Corresponding Authors

Bairui Tao − *College of Communications and Electronics Engineering, Qiqihar University, Qiqihar, Heilongjiang 161006, China; Suihua Univ, Suihua, Heilongjiang 152061, China;* orcid.org/0000-0003-0144-7691; Email: Tbr_sir@163.com

Fengjuan Miao − *College of Communications and Electronics Engineering, Qiqihar University, Qiqihar, Heilongjiang*

https://doi.org/10.1021/acs.langmuir.5c02969
Langmuir 2025, 41, 30982−30993

161006, China; orcid.org/0000-0003-4489-2322; Email: miaofengjuan@163.com

Peng Zhang − *College of Communications and Electronics Engineering, Qiqihar University, Qiqihar, Heilongjiang 161006, China*; Email: Zhangpeng@qqhru.edu.cn

Authors

Chengyu Tao − *College of Communications and Electronics Engineering, Qiqihar University, Qiqihar, Heilongjiang 161006, China*

Paul K. Chu − *Department of Physics, Department of Materials Sciences and Engineering, and Department of Biomedical Engineering, City University of Hong Kong, Kowloon, Hong Kong 999077, China*; orcid.org/0000-0002-5581-4883

Complete contact information is available at: https://pubs.acs.org/10.1021/acs.langmuir.5c02969

Author Contributions

‖B.T. and C.T. contributed equally to this work.

Notes

The authors declare no competing financial interest.

■ ACKNOWLEDGMENTS

We would like to thank the Engineering Research Center of Agricultural Multi-Dimensional Sensor Information Perception, Heilongjiang Province, and Heilongjiang Provincial Key Laboratory of Micro-Nano Sensor Component. This work was jointly supported by Program for Young Talents of Basic Research in Universities of Heilongjiang Province(YQJH2024261), Fundamental Research Funds in Heilongjiang Provincial Universities (No.145309802), Heilongjiang Science Foundation Project (No. LH2023F052), Heilongjiang Province University Discipline Collaborative Innovation Achievement Project (No. LJGXCG2023-070), and City University of Hong Kong Donation Research Grants (DONRMG Nos. 9229021 and 9220061).

■ REFERENCES

(1) Abel, E. D.; Gloyn, A. L.; Evans-Molina, C.; et al. Diabetes mellitus—Progress and opportunities in the evolving epidemic[J]. *Cell* **2024**, *187* (15), 3789−3820.

(2) Kazmi, B.; Sadiq, T.; Taqvi, S. A. A.; et al. Towards a sustainable future: Bio-hydrogen production from food waste for clean energy generation[J]. *Process Saf. Environ. Prot.* **2024**, *183*, 555−567.

(3) Kang, K. N.; Kim, S. I.; Yoon, J. C.; et al. Bi-functional 3D-NiCu-Double hydroxide@ partially etched 3D-NiCu catalysts for non-enzymatic glucose detection and the hydrogen evolution reaction[J]. *ACS Appl. Mater. Interfaces* **2022**, *14* (29), 33013−33023.

(4) Jing, Y.; Chang, S. J.; Chen, C. J.; et al. Glucose monitoring sensors: History, principle, and challenges[J]. *J. Electrochem. Soc.* **2022**, *169* (5), No. 057514.

(5) Mohamad Nor, N.; Ridhuan, N. S.; Abdul Razak, K. Progress of enzymatic and non-enzymatic electrochemical glucose biosensor based on nanomaterial-modified electrode[J]. *Biosensors* **2022**, *12* (12), No. 1136.

(6) Saha, T.; Del Caño, R.; Mahato, K.; et al. Wearable electrochemical glucose sensors in diabetes management: a comprehensive review[J]. *Chem. Rev.* **2023**, *123* (12), 7854−7889.

(7) Ishaq, H.; Dincer, I.; Crawford, C. A review on hydrogen production and utilization: Challenges and opportunities[J]. *Int. J. Hydrogen Energy* **2022**, *47* (62), 26238−26264.

(8) Lin, T. W.; Liu, C. J.; Dai, C. S. Ni3S2/carbon nanotube nanocomposite as electrode material for hydrogen evolution reaction in alkaline electrolyte and enzyme-free glucose detection[J]. *Appl. Catal. B* **2014**, *154*, 213−220.

(9) Xu, R.; Xu, D.; Zeng, Z.; et al. $CoFe_2O_4$/porous carbon nanosheet composites for broadband microwave absorption[J]. *Chem. Eng. J.* **2022**, *427*, No. 130796.

(10) Zhang, S.; Niu, H.; Cai, Y.; et al. Arsenite and arsenate adsorption on coprecipitated bimetal oxide magnetic nanomaterials: $MnFe_2O_4$ and $CoFe_2O_4$[J]. *Chem. Eng. J.* **2010**, *158* (3), 599−607.

(11) Zhu, J.; Xiao, Y.; Hu, W.; et al. A portable self-powered electrochemical sensor based on zinc-air battery for detection of hydrogen sulfide[J]. *Anal. Chem.* **2024**, *96* (5), 1852−1860.

(12) Li, Z.; Wang, Y.; Fan, Z.; et al. A dual-function wearable electrochemical sensor for uric acid and glucose sensing in sweat[J]. *Biosensors* **2023**, *13* (1), No. 105.

(13) Farahmandpour, M.; Haghshenas, H.; Kordrostami, Z. Blood glucose sensing by back gated transistor strips sensitized by CuO hollow spheres and rGO[J]. *Sci. Rep.* **2022**, *12* (1), No. 21872.

(14) Thakkar, H. K.; Joshi, K. K.; Pataniya, P. M.; et al. Photosensitive CuS/NiO heterostructure electrocatalysts for energy-saving hydrogen evolution reaction at all pH conditions[J]. *Int. J. Hydrogen Energy* **2023**, *48* (97), 38266−38278.

(15) Sharifianjazi, F.; Moradi, M.; Parvin, N.; et al. Magnetic $CoFe_2O_4$ nanoparticles doped with metal ions: a review[J]. *Ceram. Int.* **2020**, *46* (11), 18391−18412.

(16) Shen, J.; Zhang, Y.; Chen, D.; et al. A hollow CuS nanocube cathode for rechargeable Mg batteries: effect of the structure on the performance[J]. *J. Mater. Chem. A* **2019**, *7* (37), 21410−21420.

(17) Liu, Y.; Ying, Y.; Mao, Y.; et al. CuO nanosheets/rGO hybrid lamellar films with enhanced capacitance[J]. *Nanoscale* **2013**, *5* (19), 9134−9140.

(18) Zhong, Y.; Hu, Y.; Mo, H.; et al. Facilitation of PdPb nanoalloy anchored on rGO/MOF-derived δ-Ga2O3 nanorod for electrocatalytic oxidation of methanol, ethanol and ethylene glycol[J]. *Electrochim. Acta* **2022**, *408*, No. 139935.

(19) Yang, Z.; Li, H.; Feng, S.; et al. Multiform sulfur adsorption centers and copper-terminated active sites of nano-CuS for efficient elemental mercury capture from coal combustion flue gas[J]. *Langmuir* **2018**, *34* (30), 8739−8749.

(20) Gengenbach, T. R.; Major, G. H.; Linford, M. R.; Easton, C. D. Practical guides for x-ray photoelectron spectroscopy (XPS): Interpreting the carbon 1s spectrum. *J. Vac. Sci. Technol., A* **2021**, *39* (1), No. 013204, DOI: 10.1116/6.0000682.

(21) Vargas-Villanueva, S.; Torres-Ceron, D. A.; Amaya-Roncancio, S.; et al. Study of the incorporation of S in TiO2/$SO_4$2− Coatings produced by PEO process through XPS and DFT[J]. *Appl. Surf. Sci.* **2022**, *599*, No. 153811.

(22) Belgibayeva, A.; Rakhatkyzy, M.; Adi, A.; et al. Synthesis of Free-Standing CoxP/Co3 (PO_4) 2/C Composite Nanofiber Mats and Their Characteristics as Multi-functional Interlayers for Lithium-Sulfur Batteries[J]. *ChemElectroChem* **2022**, *9* (17), No. e202200458.

(23) Dang, R.; Xu, X.; Xie, M. Fabrication of triangular Cu3P nanorods on Cu nanosheets as electrocatalyst for boosted electrocatalytic water splitting[J]. *J. Cent. South Univ.* **2022**, *29* (12), 3870−3883.

(24) Zhang, R.; Song, C. Y.; Sui, Z.; et al. Recent Advances in Carbon-Nitrogen/Carbon-Oxygen Bond Formation Under Transition-Metal-Free Conditions[J]. *Chem. Rec.* **2023**, *23* (5), No. e202300020.

(25) Tao, B.; Li, J.; Miao, F.; et al. Carbon cloth loaded NiCo 2 O 4 nano-arrays to construct Co-MOF@ GO nanocubes: A high-performance electrochemical sensor for non-enzymatic glucose[J]. *IEEE Sens. J.* **2022**, *22* (14), 13898−13907.

(26) Xing, Z.; Sun, Y.; Xie, X.; et al. Zincophilic electrode interphase with appended proton reservoir ability stabilizes Zn metal anodes[J]. *Angew. Chem., Int. Ed.* **2023**, *62* (5), No. e202215324.

(27) Chen, S.; Ji, D.; Chen, Q.; et al. Coordination modulation of hydrated zinc ions to enhance redox reversibility of zinc batteries[J]. *Nat. Commun.* **2023**, *14* (1), No. 3526.

(28) Goran, J. M.; Mantilla, S. M.; Stevenson, K. J. Influence of surface adsorption on the interfacial electron transfer of flavin adenine dinucleotide and glucose oxidase at carbon nanotube and nitrogen-doped carbon nanotube electrodes[J]. *Anal. Chem.* **2013**, *85* (3), 1571−1581.
(29) Zeng, Z.; Mei, B. A.; Song, G.; et al. Physical interpretation of the electrochemical impedance spectroscopy (EIS) characteristics for diffusion-controlled intercalation and surface-redox charge storage behaviors[J]. *J. Energy Storage* **2024**, *102*, No. 114021.
(30) Zafar, H.; Channa, A.; Jeoti, V.; et al. Comprehensive review on wearable sweat-glucose sensors for continuous glucose monitoring[J]. *Sensors* **2022**, *22* (2), No. 638.
(31) Kang, K. N.; Kim, S. I.; Yoon, J. C.; et al. Bi-functional 3D-NiCu-double hydroxide@ partially etched 3D-NiCu catalysts for non-enzymatic glucose detection and the hydrogen evolution reaction[J]. *ACS Appl. Mater. Interfaces* **2022**, *14* (29), 33013−33023.
(32) Bhuvaneswari, C.; Babu, S. G. Nanoarchitecture and surface engineering strategy for the construction of 3D hierarchical CuS-rGO/g-C3N4 nanostructure: an ultrasensitive and highly selective electrochemical sensor for the detection of furazolidone drug[J]. *J. Electroanal. Chem.* **2022**, *907*, No. 116080.
(33) Gao, F.; Yang, Y.; Qiu, W.; et al. Ni3C/Ni nanochains for electrochemical sensing of glucose[J]. *ACS Appl. Nano Mater.* **2021**, *4* (8), 8520−8529.
(34) Xu, J.; Chen, T.; Qiao, X.; et al. The hybrid of gold nanoparticles and Ni (OH) 2 nanosheet for non-enzymatic glucose sensing in food[J]. *Colloids Surf., A* **2019**, *561*, 25−31.
(35) Ramasamy, R.; Ramachandran, K.; Philip, G. G.; et al. Design and development of Co3O4/NiO composite nanofibers for the application of highly sensitive and selective non-enzymatic glucose sensors[J]. *RSC Adv.* **2015**, *5* (93), 76538−76547.
(36) Salarizadeh, P.; Rastgoo-Deylami, M.; Askari, M. B. Electrochemical properties of Ni3S2@ MoS2-rGO ternary nanocomposite as a mising cathode for Ni−Zn batteries and catalyst towards hydrogen evolution reaction[J]. *Renewable Energy* **2022**, *194*, 152−162.
(37) Yuan, C.; Lv, H.; Zhang, Y.; et al. Three-dimensional nanoporous heterojunction of CdS/np-rGO for highly efficient photocatalytic hydrogen evolution under visible light[J]. *Carbon* **2023**, *206*, 237−245.

https://doi.org/10.1021/acs.langmuir.5c02969
Langmuir 2025, 41, 30982−30993